SPHERIC 2022

CATANIA, ITALY, 6–9 JUNE 2022

Proceedings of the 16th SPHERIC International Workshop

Edited by
Giuseppe Bilotta

SPHERIC 2022

Proceedings of the 16th SPHERIC International Workshop

Catania, Italy, 6–9 June 2022
Istituto Nazionale di Geofisica e Vulcanologia
Università di Catania

Edited by
Giuseppe Bilotta

Published by the Istituto Nazionale di Geofisica e Vulcanologia
ISBN 979-12-8028-205-7

Acknowledgements

The 16th SPHERIC International Workshop is supported by the Osservatorio Etneo of the Istituto Nazionale di Geofisica e Vulcanologia, the Università di Catania and ERCOFTAC.

To our colleagues from the Osservatorio Etneo, Monastero dei Benedettini, Museo della Rappresentazione and the Laboratorio di Idraulica go our deepest and sincere thanks for their logistical support. Our gratitude extends to all the members of the SPHERIC Steering Committee, and the chair and vice chair in particular, for their continued guidance in the organization of the workshop. This Workshop would not have been possible without your support.

Foreword

Dear Delegate,

the Osservatorio Etneo, Catania section of the Istituto Nazionale di Geofisica e Vulcanologia, in collaboration with the Università di Catania, is delighted to host the 16th SPHERIC International Workshop.

SPHERIC, the ERCOFTAC Special Interest Group that represents the community of researchers and industrial users of Smoothed Particle Hydrodynamics, has made outstanding efforts to support and foster the development of SPH with online and hybrid events in these difficult times, finding new and creative ways to bring people together and keep the interest for SPH alive inside and outside the community. The choice between a virtual and an on-site event for the 16th edition of the SPHERIC International Workshops has been a difficult one to make. On the one hand, the still problematic international situation would have obstructed participation; on the other, the kind and level of inter-personal exchange that can only be achieved by meeting in-person remains an important aspect of the scientific growth of the community. We have taken a gamble of sorts, and we appreciate the effort of all of you, those that have had the opportunity to come, as well as those that could not make it, in supporting our choice.

In the now well-established tradition of the SPHERIC International Workshops, the programme of this edition offers a Training Day for researchers and users that are starting their work on SPH, and two challenging keynotes. As usual, the Libersky Prize will be awarded for the best contribution from student delegates; the 16th SPHERIC International Workshop also presents for the third time the Joe Monaghan Prize, a recognition to the most important work published on the SPHERIC Grand Challenges between 2013 and 2018.

The contributions that you can find in these Proceedings were selected by our Scientific Committee from over 80 high-level proposed abstracts. They are a testament to the excellent quality of the research being conducted both on the fundamentals of the SPH method and on its application to a wide variety of fields, from engineering to medicine, from geophysics to material sciences.

New and exciting times await Smoothed Particle Hydrodynamics and the SPHERIC community, and it is a great pleasure and honour to share these moments with you.

Come for the science, stay for the food!
Welcome to Catania,

Giuseppe Bilotta
Chair, Local Organizing Committee
16th SPHERIC International Workshop

Scientific Committee

Dr. Alex Crespo (Universidade de Vigo, Ourense, Spain)
Dr. Abbas Khayyer (Kyoto University, Japan)
Dr. David Le Touzé (Ecole Centrale de Nantes, France)
Dr. Nathan Quinlan (National University of Ireland, Galway, Ireland)
Dr. Stefano Sibilla (Università di Pavia, Italy)
Dr. Angelo Tafuni (New Jersey Institute of Technology, US)
Dr. Renato Vacondio (Università di Parma, Italy)
Dr. Antonio Gil (Swansea University, UK)
Dr. Andrea Colagrossi (CNR-INM, Italy)
Dr. Ben Rogers (University of Manchester, UK)
Dr. Salvatore Marrone (CNR-INM, Italy)
Dr. Peter Eberhard (University of Stuttgart, Germany)
Dr. Matthieu De Leffe (Siemens Digital Industries, France)
Dr. Giuseppe Bilotta (Istituto Nazionale di Geofisica e Vulcanologia, Italy)
Dr. Ha Bui (Monash University, Australia)
Dr. Raj Das (RMIT University, Australia)
Dr. Steven Lind (University of Manchester, UK)
Dr. Georgios Fourtakas (University of Manchester, UK)
Dr. Chun Hean Lee (Universiy of Glasgow, UK)
Dr. Moncho Gómez-Gesteira (Universidade de Vigo, Spain)
Dr. Xu Fei (Northwestern Polytechnical University, China)
Dr. Antonio Souto Iglesias (UPM, Spain)
Dr. Rouhollah Fatehi (Persian Gulf University, Iran)
Dr. Xiangyu Hu (Technical University of Munich, Germany)
Dr. Pengnan Sun (Sun Yat-sen University, China)
Dr. Tom De Vuyst (University of Hertfordshire, UK)

Local Organizing Committee

Dr. Giuseppe Bilotta
Dr. Annalisa Cappello
Dr. Gaetana Ganci

Table of contents

Convergence, consistency and stability I (S1)

Boundary Conditions (S2)

Solids and structures (S3)

Alternative and novel formulations (S4)

Practical and industrial applications I: automotive and aerospace engineering (S5)

Convergence, consistency and stability II (S6)

Viscosity and turbulence (S10)

Complex physics (S11)

Adaptivity, efficiency and acceleration (S12)

SPH in software: preprocessing, post-processing and high-performance computing (S13)

Practical and industrial applications III: thin film mechanics (S14)

Weakly-compressible SPH schemes with an acoustic-damper term

Peng-Nan Sun
School of Ocean Engineering and Technology
Sun Yat-sen University
Zhuhai, 519000, China

Chiara Pilloton, Matteo Antuono, Andrea Colagrossi
CNR, National Research Council of Italy
INM, Institute of marine engineering
Rome, 00128, Italy
matteo.antuono@cnr.it

***Abstract*—Spurious pressure and density waves often occur in weakly-compressible SPH simulations and their propagation and reflection from the boundaries generally lead to large oscillations in the pressure field and noise in the measured loads on solid structures. In the present work this problem is tackled by adding an artificial damping term for acoustic waves in the momentum equation, as theoretically proposed in [1]. Similarly to other diffusive terms previously proposed for weakly-compressible SPH schemes, the present acoustic damper term converges to zero when the particle resolution increases, proving to be numerically consistent. Numerical results show that the acoustic damper is effective in removing the spurious acoustic noise.**

I. Introduction

In the last decade the SPH model has been widely applied to simulate free-surface flows and water wave impacts (see *e.g.* [2]–[8]). Among the different SPH schemes, the weakly-compressible variants (namely, the SPH models defined through the use of a reduced sound speed in comparison to the actual one) are widely employed, thanks to their simple code structure and the easier implementation of parallel computing. The main drawback of the weakly-compressible SPH schemes is, however, the presence of spurious acoustic waves generated by the assumption that the fluid is weakly-compressible. Although different pressure stabilization techniques are cooperated with the weakly-compressible SPH models (see *e.g.* density filters [9], diffusive terms [10] and Riemann solvers [11]), spurious pressure waves are still observed in the free-surface flows with violent impacts. For example, in the simulations of violent fluid-solid interactions, strong liquid impacts on the structure generate a group of pressure waves (see *e.g.* [12]–[14]) whose reflection at the boundaries of the fluid domain causes nonphysical loads to the structure. SPH simulations of sloshing flows with periodical free-surface impacts on solid walls is another example where large pressure oscillations are induced in the flow (see *e.g.* [15]). It is possible to show that the solution of a weakly-compressible fluid can be decomposed in an "incompressible-flow" component plus an acoustic part which are superimposed in a complex and non-linear way. Unfortunately, it is not possible to filter out the acoustic component in a straightforward way, so that in some works a post-processing filtering procedure is proposed [15]. In fact, techniques like the density filters, diffusive terms and Riemann solvers are essentially proposed to prevent high-frequency pressure oscillations and they are mainly effective at length scales comparable to the kernel radius. Conversely, the pressure waves generated by the reduced sound speeds are characterized by a larger scale and lower frequency and, consequently, they are only partially prevented by the existing techniques. The aim of the present work is, then, to define a novel diffusive term specifically conceived to damp such acoustic oscillations. The basic idea is borrowed from the work of [1] where an appropriate dissipation function that depends on the rate of change of particle volume is introduced. The latter approach leads to the appearance of an "acoustic damper" term inside the momentum equation that preserves both linear and angular momenta and that is purely dissipative (namely, it gives a negative-define contribution to the energy balance). Thanks to its simple structure, the proposed "acoustic damper" term can be implemented in a generic weakly-compressible SPH model straightforwardly. In the present work we principally apply it to the δ^+-SPH scheme, since the latter represents the most recent and promising advancement of the δ-SPH model. The present work is structured as follows: in Section §II we introduce the δ^+-SPH scheme and describe the proposed acoustic-damper term. In particular, Sections §II-A and §II-B clarify some details about the integration scheme and the conservation of energy. Finally, Section §III shows the results obtained by using the acoustic damper term in the weakly-compressible SPH schemes.

II. The adopted δ^+-SPH scheme with acoustic damper term

In the present section we briefly introduce the δ^+-SPH scheme defined in [16] and further inspected in [17] which is the reference model for the simulations shown in the sequel. Hereinafter the fluid is assumed to be compressible and barotropic, *i.e.* the pressure field depends on the density field through a suitable state equation. Since the variations of the density field are supposed to be small for a liquid phase, the state equation is linearized around a reference density state, ρ_0, which generally refers to the density along the free surface $p = c_0^2\,(\rho - \rho_0)$ where c_0 is the speed of sound. The weakly-compressible regime implies the following requirement:

$$c_0 \geq \max\left(10U_{max}\,, 10\sqrt{\frac{(\Delta p)_{max}}{\rho}}\right) \tag{1}$$

where U_{max} and $(\Delta p)_{max}$ are respectively the maximum fluid speed and the maximum pressure variation (with respect to the pressure on the free-surface) expected in the fluid domain (see *e.g.* [18]). To avoid too small time steps in numerical simulations, c_0 is usually chosen smaller than its physical value. The constraint (1), however, has to be satisfied to guarantee the weakly-compressible regime and this condition has to be verified throughout the simulations. In the δ^+-SPH scheme the particle masses m_i are assumed to be constant during their motion. The particles are set initially on a lattice with homogeneous spacing Δr, and hence, the particles' volumes V_i are evaluated initially as Δr^2 and the particle masses m_i are calculated through the initial density field (using the equation of state and the initial pressure field). During the time evolution volumes V_i change in time accordingly with particle density ρ_i. For the sake of brevity, in the following text the notation $\boldsymbol{r}_{ji}$ indicates the differences of the particles positions $(\boldsymbol{r}_j - \boldsymbol{r}_i)$ and the same holds for the velocity fields $\boldsymbol{u}_{ji}$ and $\delta\boldsymbol{u}_{ji}$, while, for the generic scalar field the notation f_{ij} just indicates the dependency of the field f on the indices i and j. The spatial gradients are approximated through convolution summations with a kernel function W_{ij}. As in [19] a C2-Wendland kernel [20] is adopted in the present work. Regarding the spatial derivative of W, due to its properties, it is possible to write:

$$\nabla_i W_{ij} \,=\, \boldsymbol{r}_{ji}\, F_{ij} \tag{2}$$

where the scalar function F_{ij} only depends on the particle distance $r_{ji} = \|\boldsymbol{r}_{ji}\|$ and it is strictly positive (see *e.g.* [21]). The δ^+-SPH equations adopted in this work read as:

$$\begin{cases} \dfrac{\mathrm{d}\rho_i}{\mathrm{d}t} &= -\rho_i \displaystyle\sum_j (\boldsymbol{u}_{ji} + \delta\boldsymbol{u}_{ji}) \cdot \nabla_i W_{ij}\, V_j \\ & \quad + \displaystyle\sum_j (\rho_j\, \delta\boldsymbol{u}_j + \rho_i\, \delta\boldsymbol{u}_i) \cdot \nabla_i W_{ij}\, V_j \,+ \mathcal{D}^\rho_i \\ \rho_i \dfrac{\mathrm{d}\boldsymbol{u}_i}{\mathrm{d}t} &= \boldsymbol{F}^p_i \,+\, \boldsymbol{F}^v_i \,+ \boldsymbol{F}^{ad}_i \,+\, \rho_i \boldsymbol{g} \\ & \quad + \displaystyle\sum_j (\rho_j\, \boldsymbol{u}_j \otimes \delta\boldsymbol{u}_j + \rho_i\, \boldsymbol{u}_i \otimes \delta\boldsymbol{u}_i) \cdot \nabla_i W_{ij}\, V_j \\ \dfrac{\mathrm{d}\boldsymbol{r}_i}{\mathrm{d}t} &= \boldsymbol{u}_i + \delta\boldsymbol{u}_i, \quad V_i = m_i \,/\rho_i, \quad p = c_0^2(\rho - \rho_0), \end{cases} \tag{3}$$

where the indexes i and j refer to generic i-th and j-th particles, $\boldsymbol{F}^p_i$ and $\boldsymbol{F}^v_i$ are the pressure and viscous forces acting on the particle i. The vector $\delta\boldsymbol{u}$ is the Particle Shifting velocity adopted to regularize the particles' spatial distribution during their motion. The force field $\boldsymbol{F}^{ad}_i$ is the proposed term conceived to damp the acoustic waves. More details are given at the end of this section. The time derivative d/dt used in (3) indicates a quasi-lagrangian derivative, *i.e.*:

$$\frac{d(\bullet)}{dt} \,:=\, \frac{\partial(\bullet)}{\partial t} \,+\, \nabla(\bullet) \cdot (\boldsymbol{u} + \delta\boldsymbol{u})\,,$$

since the particles are moving with the modified velocity $(\boldsymbol{u} + \delta\boldsymbol{u})$ and the above equations are written in an Arbitrary-Lagrangian-Eulerian framework. For this reason the continuity and the momentum equations contain terms with spatial derivatives of $\delta\boldsymbol{u}$ (for details see [17]). The term $\mathcal{D}^\rho_i$ is the numerical diffusive term introduced by [22] to filter out the spurious high-frequency noise in the pressure field. Following [19] this term is rewritten as follows:

$$\begin{cases} \mathcal{D}^\rho_i &:= \;\; \delta\, c_0\, h \displaystyle\sum_j \psi_{ji}\, F_{ij}\, V_j\,, \\ \psi_{ji} &:= \;\; 2\left[(\rho_j - \rho_i) - \dfrac{1}{2}\left(\langle\nabla\rho\rangle^L_i + \langle\nabla\rho\rangle^L_j\right) \cdot \boldsymbol{r}_{ji}\right] \end{cases} \tag{4}$$

where δ is a dimensionless constant set equal to 0.1 while $2h = 4\Delta r$ is the support of the C2-Wendland kernel W. The superscript L in (4) indicates that the gradient is evaluated through the renormalized gradient equation, *i.e.*:

$$\langle\nabla\rho\rangle^L_i \,=\, \sum_j (\rho_j - \rho_i)\, \mathbb{L}^{-1}_i\, \nabla_i W_{ij}\, V_j\,, \tag{5}$$

$$\mathbb{L}_i := \left[\sum_k (\boldsymbol{r}_{ki} \,\otimes\, \boldsymbol{r}_{ki})\, F_{ik}\, V_k\right] \tag{6}$$

where $\mathbb{L}_i$ is the renormalization matrix (see *e.g* [10]). Regarding the pressure force $\boldsymbol{F}^p$, following the work by [23] this is expressed as:

$$\begin{cases} \boldsymbol{F}^p_i \,=\, -\displaystyle\sum_i \,(p_j \,+\, p_i)\, \nabla_i W_{ij}\, V_j \,+\, S_i \sum_j \nabla_i W_{ij}\, V_j \\ S_i \,= \begin{cases} 0 & p_i \geq 0 \\ 2p_i & p_i < 0 \quad i \notin \mathscr{S}_F \end{cases} \end{cases} \tag{7}$$

where $\mathscr{S}_F$ denotes the region of the fluid domain close to the free surface, that is the free-surface particles and their neighbouring particles. The free-surface particles are detected through the algorithm described in [24]. The term S_i inside the Eq. (7) corresponds to a switch from the "plus" formulation (namely, $p_j + p_i$) to the minus formulation (that is, $p_j - p_i$) in the fluid regions where the pressure p_i is negative. This switch allows removing the so-called "tensile instability" which is a numerical instability of the SPH scheme (see [25], [26]).

The viscous force $\boldsymbol{F}^v$ is expressed as:

$$\boldsymbol{F}^v_i := \alpha\, \rho_0\, c_0\, h\, \sum_j \pi_{ij}\, \nabla_i W_{ij}\, V_j\,, \qquad \pi_{ij} := \frac{\boldsymbol{u}_{ji} \cdot \boldsymbol{r}_{ji}}{||\boldsymbol{r}_{ji}||^2} \tag{8}$$

where α is a dimensionless constant which determines the intensity of the artificial viscous force. It is linked to the equivalent dynamic viscosity through the relation $\mu = \alpha\, \rho_0\, c_0\, h/[2(n+2)]$ where n is the number of spatial dimensions (see *e.g.* [27]). Finally, the artificial acoustic damper force $\boldsymbol{F}^{ad}$ is given by the formula below:

$$\boldsymbol{F}_i^{ad} = \alpha_2\,\rho_0\,c_0\,h\,\sum_j (\,\dot{c}_j + \dot{c}_i\,)\;\nabla_i W_{ij}\,V_j\,, \qquad (9)$$

where $\dot{c}_k = -\dot{\rho_k}/\rho_k = \sum_l \boldsymbol{u}_{lk}\cdot\nabla_k W_{kl}\,V_l$. The intensity of this new term is tuned with the dimensionless parameter α_2 similarly to the viscous parameter α in Eq. (8). The acoustic damper term is defined following the work of [1] where an appropriate dissipation function that depends on the rate of change of particle volume is introduced. Remarkably, such a term preserves both linear and angular momenta. The Particle Shifting velocity $\delta\boldsymbol{u}$ in Eq. (3) is given by:

$$\begin{cases} \delta\boldsymbol{u}_i^* = -\xi\,h\,U_{\max}\sum_j \left[1+R\left(\dfrac{W_{ij}}{W(\Delta r)}\right)^n\right]\nabla_i W_{ij}\,V_j\,. \\[2ex] \delta\boldsymbol{u}_i = \min\left(\|\delta\boldsymbol{u}_i^*\|, \dfrac{\max_j \|\boldsymbol{u}_{ij}\|}{2}, \dfrac{U_{\max}}{2}\right)\dfrac{\delta\boldsymbol{u}_i^*}{\|\delta\boldsymbol{u}_i^*\|} \end{cases} \qquad (10)$$

Here, the constants R and n are respectively set to 0.2 and 4 as in [16], [28]. Since the first expression in equation (10) is proportional to the smoothing length, the intensity of $\delta\boldsymbol{u}$ reduces as the spatial resolution increases, and this guarantees that $\delta\boldsymbol{u}_i$ induces small deviations with respect to the physical particle trajectory. The second equation in (10) is introduced to limit the magnitude of the shifting velocity for the purposes of robustness. Regarding the dimensionless constant ξ, this is set equal to 1, unless otherwise specified. In fact, through the analysis of the energy associated with the PST (see Section §II-B), we found that for the simulations at high spatial resolution presented in Section III-B, the constant ξ can be reduced (with a consequent decreasing of the $\delta\boldsymbol{u}$ magnitude), retaining the full benefits of the PST. As documented in [16], the use of the Particle Shifting Technique (PST) leads to regular particle distributions and increases the accuracy and the robustness of the scheme. In turn, the inclusion of the PST causes the loss of the exact conservation of the angular momenta as commented in [16] and in [17]. It is worth noting that the shifting velocity close to the free surface has to be modified to be consistent with the kinematic boundary condition along such an interface. In particular, the normal component of $\delta\boldsymbol{u}$ to the free surface is nullified while the tangential component is maintained unaltered (for more details (see [16] or [29]).

A. Time integration

The system (3) is integrated in time by using a fourth-order Runge-Kutta scheme with frozen diffusion as described in [10]. The use of a frozen-diffusion algorithm allows for a restrained computational cost and its coupling with the fourth-order Runge-Kutta scheme proves to be stable, robust and reliable. The same approach is also applied to the vector $\delta\boldsymbol{u}$ vector which is kept constant during the Runge-Kutta sub-steps. Despite a double loop on all the particles is required for the evaluation of the acoustic damper term, the extra CPU-costs for performing this double loop remains rather limited in our code. The time step for the integration, Δt, is obtained as the minimum over the following bounds:

$$\begin{cases} \Delta t_v = \dfrac{1}{\alpha}\left(\dfrac{h}{c_0}\right), \quad \Delta t_a = 0.25\,\min\limits_i \sqrt{\dfrac{h}{\|\boldsymbol{a}_i\|}}\,, \\[2ex] \Delta t_\delta = \dfrac{0.44}{\delta}\left(\dfrac{h}{c_0}\right), \quad \Delta t_c = K_c\left(\dfrac{h}{c_0}\right), \quad \Delta t_{ad} = \dfrac{K_c}{\alpha_2}\left(\dfrac{h}{c_0}\right), \\[2ex] K_c = 1.5 \qquad \Delta t = \min(\Delta t_v\,, \Delta t_a\,, \Delta t_\delta\,, \Delta t_c\,, \Delta t_{ad}) \end{cases} \qquad (11)$$

where $\|\boldsymbol{a}_i\|$ is the particle acceleration and the Courant-Friedrichs-Lewy constants have been found heuristically. It is worth noting that these constants are valid for the present scheme and for the chosen kernel funtion (i.e. the C2-Wendland kernel). Since we are interested in problems involving water impacts, the Reynolds number is generally high and, consequently, α is rather small, ranging from 0 to 0.01. This implies that the constraint on Δt_v is the least restrictive. Similarly, the constraint on Δt_δ is always negligible since δ is fixed to 0.1 (see also [22]). Conversely, the coefficient α_2 has to be large enough in order to damp of the acoustic waves generated during impact events and, at the same time, it has to be smaller than unity to avoid that Δt_{ad} becomes smaller than Δt_a and Δt_c. Generally, Δt_c represents the most restrictive condition and the choice of K_c is fundamental for the stability and accuracy of the adopted numerical model. For δ^+-SPH , $K_c = 1.5$ proves be a reliable choice, while $K_c = 1.3$ and $K_c = 1.0$ are suitable for the δ-SPH and for the Standard SPH model respectively when the acoustic damper is implemented. These latter schemes, however, are not shown in the present work.

B. Energy conservation within the adopted SPH model

Following the analysis performed in [30] and in [31], we provide the energy balance for the particle system presented in the previous section. This can be briefly arranged as follows:

$$\dot{\mathcal{E}}_M + \dot{\mathcal{E}}_C - \mathcal{P}_{ext} = \mathcal{P}_V + \mathcal{P}_{ad} + \mathcal{P}_{\mathcal{N}} \qquad (12)$$

where $\mathcal{E}_M$ is the mechanical energy of the particle system, composed of the kinetic energy $\mathcal{E}_K = \sum_i m_i\,\|\boldsymbol{u}_i\|^2/2$ and the potential energy $\mathcal{E}_P = \sum_i m_i\,g\,z_i$ (z_i being the vertical coordinate of the i-th particle), whereas $\mathcal{E}_C$ is the elastic potential energy:

$$\mathcal{E}_C = \mathcal{E}_C(\rho_0) + c_0^2\sum_j \left[\log\left(\frac{\rho_j}{\rho_0}\right) + \frac{\rho_0}{\rho_j} - 1\right]\rho_j\,dV \quad (13)$$

The external power $\mathcal{P}_{ext}$ is evaluated through the mutual interaction between fluid and solid particles, as detailed in [30] and [32]. Following the latter work, the power related to fluid-fluid particles interactions of the viscous forces is :

$$\mathcal{P}_V = -\frac{\alpha\,\rho_0\,c_0\,h}{2}\sum_i\sum_j(\pi_{ij}\,r_{ij})^2\,F_{ij}\,V_i\,V_j\,, \qquad (14)$$

The positiveness of the function F_{ij} guarantees that this is a pure dissipation term (for more details see *e.g.* [21]). The contribution related to the "acoustic damper" is equal to:

$$\mathcal{P}_{ad} \;=\; -\,\alpha_2\,\rho_0\,c_0\,h\sum_i \dot{c}_i^2\,V_i \tag{15}$$

where the right-hand side has been obtained by using the symmetric properties of the kernel function (2). Similarly to $\mathcal{P}_V$, $\mathcal{P}_{ad}$ is a purely dissipation term. It is worth noting that $\mathcal{P}_N$ is not a strictly dissipation term, although it includes the energy contributions from the pressure switch and the PST which guarantee the stability of the numerical scheme even when α and α_2 are zero. The energy dissipated by the scheme, $\mathcal{E}_{diss}$, can be expressed as:

$$\begin{cases} \mathcal{E}_{diss} \,=\, \mathcal{E}_V \,+\, \mathcal{E}_{ad} \,+\, \mathcal{E}_N\,, \\[2ex] \mathcal{E}_V := \displaystyle\int_{t_0}^{t}\mathcal{P}_V\,dt\,, \quad \mathcal{E}_{ad} := \displaystyle\int_{t_0}^{t}\mathcal{P}_{ad}\,dt\,, \quad \mathcal{E}_N := \displaystyle\int_{t_0}^{t}\mathcal{P}_N\,dt\,. \end{cases} \tag{16}$$

As discussed in [33], during liquid impacts a sudden energy loss occurs. The weakly-compressibility assumption, underlying the present scheme, implies that during these events a portion of the mechanical energy is converted into internal compressible energy in the form of acoustic waves. This part is mainly dissipated by numerical diffusive terms $\mathcal{E}_N$ and by the "acoustic damper" term. The remaining portion is absorbed by the energy component $\mathcal{E}_N$, as shown in [31]. This latter term becomes less important with respect to the viscous dissipation $\mathcal{P}_V$ when impacts are absent.

III. Test cases: Application of the acoustic damper term to the δ^+-SPH and δ-SPH models

In the present section we firstly consider two benchmarks for the proposed acoustic damper term. The first benchmark describes the impacts of inviscid fluid patches in absence of solid boundaries. Differently from the previous test case, these problems are characterized by an intense generation of acoustic waves and, thus, are used to prove the effectiveness of the proposed acoustic term. The second benchmark is dedicated to the evolution of a dam break flow and to its violent interaction with solid walls. Finally, the third test case is dedicated to the simulation of a water entry problem in which strong impact usually induces the generation of strong acoustic waves in weakly-compressible SPH simulations.

A. Impact of two water jets in 2D

In the present section the impact of two rectangular patches of fluid is considered, similarly to what done in [33], and the results with and without the use of the acoustic damper term are compared. The parameters used in the numerical simulations are $c_0 = 100$ m/s, $U = 1$ m/s, $\alpha = 0.001$ and $\alpha_2 = 1$ or 0. We first focus on the normal impact of two fluid patches with the same masses. The initial stages of the evolution are drawn in Figure 1. During this phase, a large number of acoustic waves are generated as a consequence of the impact and spread all over the fluid domain. As shown in the upper panels of Figure 2, the use of the acoustic damper term drastically reduces the occurrence of these waves in comparison to the version without it (bottom panels). Figure 3 shows the evolution of the total mechanical energy $\mathcal{E}_M$ and compares it to the analytical solution derived for an inviscid incompressible fluid in [33]. The behavior of the different energy contributions with (top) and without (bottom) the acoustic damper term unveils that in the former case the dissipation due to the acoustic damper term, namely $\mathcal{E}_{Ad}$, plays a major role in comparison to the term $\mathcal{E}_N$ that, on the contrary, is the principal source of dissipation in the scheme with $\alpha_2 = 0$. In particular Figure 4 shows that the presence of the acoustic damper reduces the amount of energy that is dissipated by the viscous term, namely $\mathcal{E}_V$. In general, the scheme with the acoustic damper term converges faster to the analytical solution. The convergence, however, becomes slower as the resolution increases (see Figure 5). This is a consequence of the decrease in magnitude of the acoustic damper term, as indicated by Eq. (9). Despite this, such a term is still effective at fine resolutions, because of the larger generation of acoustic frequencies after the impact. This motivates the faster convergence in comparison to the scheme without the acoustic term (see Figure 3). As a second example,

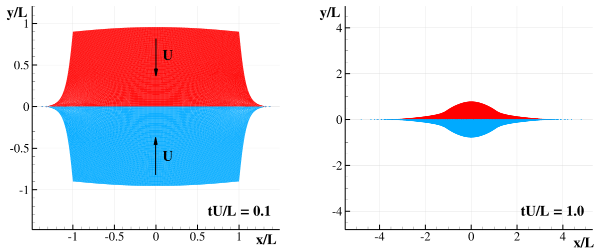

Fig. 1. Normal impact of 2D water-jets with the same masses ($L/\Delta r = 200$). Particles initially belonging to different fluid patches are plotted with different colours.

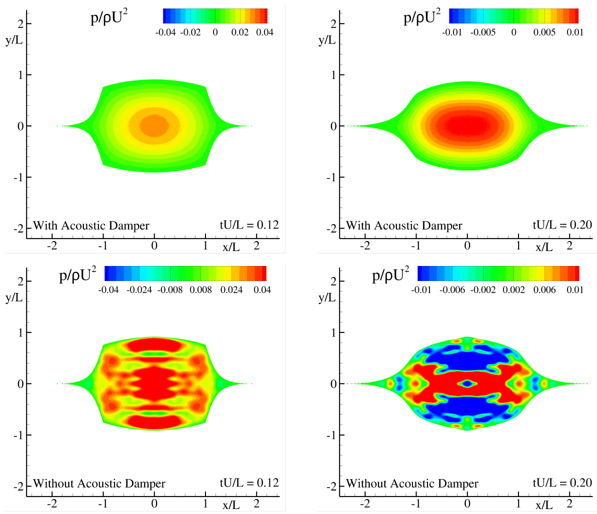

Fig. 2. Normal impact of 2D water-jets with the same masses ($L/\Delta r = 200$). Evolution of the pressure field with (top) and without (bottom) the acoustic damper term.

we deal with the normal impact of two fluid patches with different masses. Some snapshots of the initial configuration and of the subsequent evolution are sketched in Figure 6. In this case two jets generate at the extremities of the smaller patch and evolve as thin elongated filaments of fluid. The time history for three different spatial resolutions is displayed in Figure 7 along with the theoretical solution for inviscid fluid (black solid line).

B. Dam-break flow against a vertical wall

Here the effectiveness of the acoustic damper force is tested by simulating a dam-break flow impacting against a vertical wall. This is one of the most used benchmar within the SPH community and for more information and details the interested reader is addressed to [18], [34], [35]. Figure 8 shows the dam-break flow generated by the gravity collapse of a water column of height H and width 2H. The fluid is confined in a rectangular tank of length $L = 5.366H$ and height $5H$. After the break of the dam, it evolves rightwards, impacts against the tank wall and generates a reverse flow with a plunging breaking wave. During the evolution, the pressure at the probes P_1 $(y = 0.01H)$ and P_2 $(y = 0.17H)$ along the right wall is recorded. Differently from [34], the signals at the probes have not been filtered in time nor spatially averaged on the probe areas. Ten different simulations were performed with five different spatial resolutions, namely $H/\Delta r = 50, 100, 200, 400, 800$, with and without the acoustic damper term (*i.e* $\alpha_2 = 1$ and $\alpha_2 = 0$). The speed of sound is set equal to $c_0 = 20\sqrt{gH}$ and the artificial viscosity is $\alpha = 0.005$. For the highest two spatial resolutions, namely $H/\Delta r = 400$ and 800, the constant ξ in the equation (10) is reduced to 0.5 and 0.25 decreasing the intensity of the PST (see Section II). Figures 9 and 10 display some snapshots of the evolution of the pressure field with and without the use of the acoustic damper term. Remarkably, this term is able to remove the largest part of the acoustic noise not only during the initial fluid impact against the solid wall (top panels), but also during the later evolution characterized by the closure of the plunging wave cavity (middle panels) and by the subsequent splash-up cycles (bottom panels). Further, the noise-free pressure field displayed in Figure 10 allows for a clear detection of the intense vortical structures

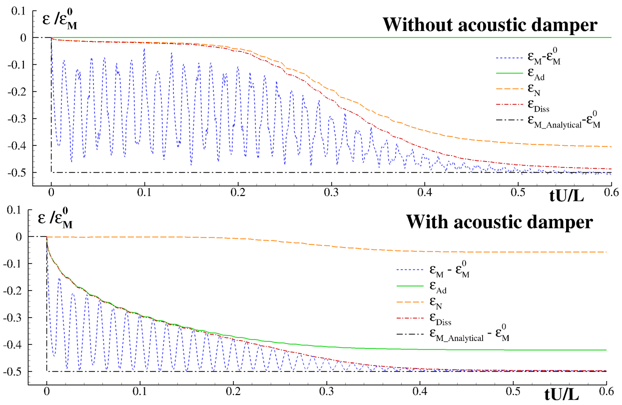

Fig. 3. Normal impact of 2D water-jets with the same masses ($L/\Delta r = 200$). Evolution of the total mechanics energy with (top) and without (bottom) the acoustic damper term. The symbol $\mathcal{E}_M^0$ denotes the global mechanical energy at the initial time.

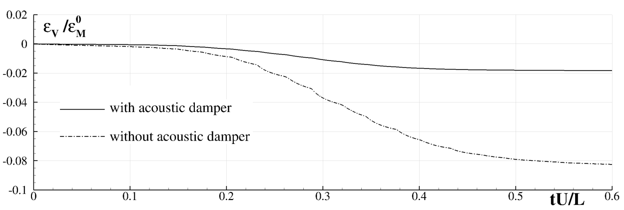

Fig. 4. Normal impact of 2D water-jets with the same masses ($L/\Delta r = 200$). Evolution of the energy related to the artificial viscous term with (solid line) and without (dashed-dotted line) the acoustic damper term.

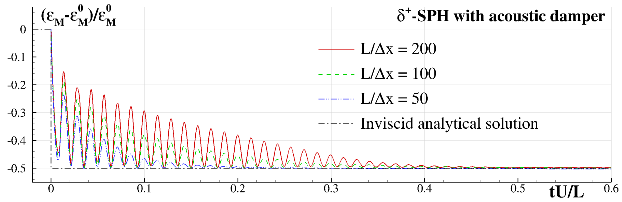

Fig. 5. Normal impact of 2D water-jets with the same masses. Evolution of the total mechanics energy with the acoustic damper term for different spatial resolutions. The symbol $\mathcal{E}_M^0$ denotes the global mechanical energy at the initial time.

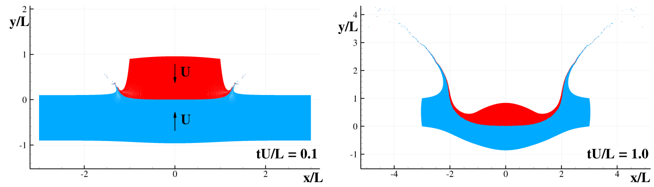

Fig. 6. Normal impact of 2D water-jets with different masses ($L/\Delta r = 200$). Particles initially belonging to different fluid patches are plotted with different colours.

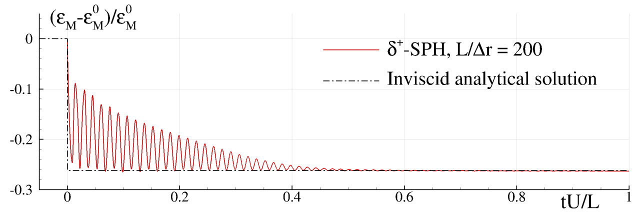

Fig. 7. Normal impact of 2D water-jets with different masses. Time evolution of the mechanical energy for three particle resolutions. The symbol $\mathcal{E}_M^0$ denotes the global mechanical energy at the initial time.

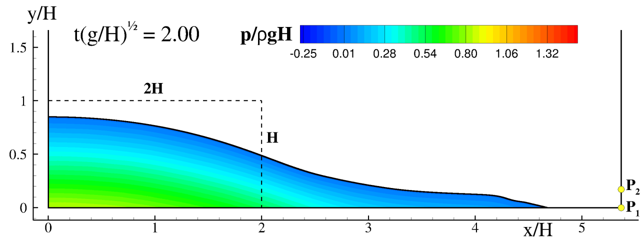

Fig. 8. Dam-break flow of a water column of height H and width $2H$ (resolution $H/\Delta r = 400$). The colors are representative of the pressure field.

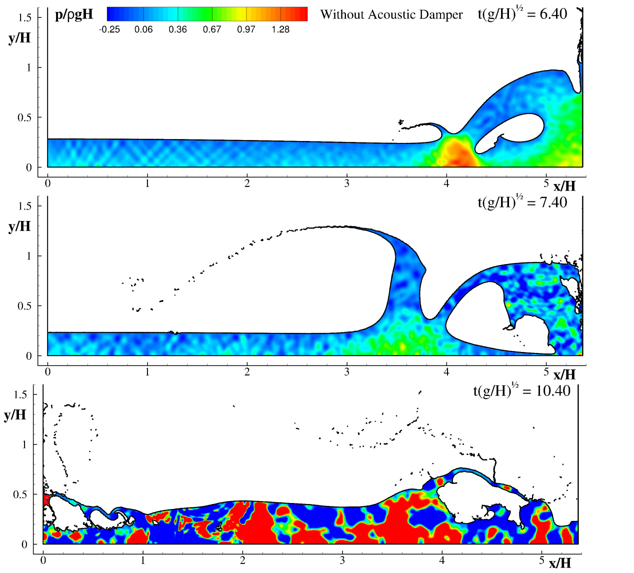

Fig. 9. Dam-break flow of a water column with $H/\Delta r = 400$, $\alpha = 0.005$, $\alpha_2 = 0.0$. The colors are representative of the pressure field.

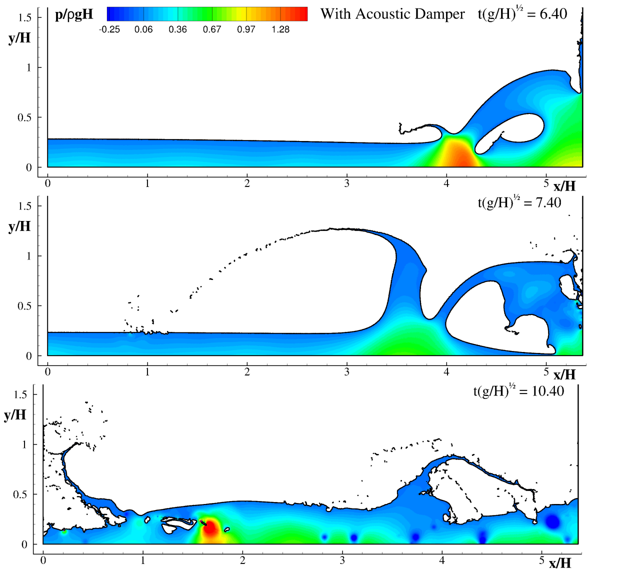

Fig. 10. Dam-break flow of a water column with $H/\Delta r = 400$, $\alpha = 0.005$, $\alpha_2 = 1.0$. The colors are representative of the pressure field.

generated by the splash-up events. The core of these eddies is characterized by an intense pressure drop (i.e. the dark blue spots in the panels at $t\sqrt{g/H} = 10.4$) which is completely hidden by acoustic waves when the acoustic damper term is not used. Figure 11 depicts the contour of the vorticity field at $t\sqrt{g/H} = 10.40$ when the above-mentioned eddies can be clearly identified. The behaviour of the scheme at different spatial resolutions is described in Figure 12 where the pressure signal at the probe P_1 is displayed with and without the acoustic damper term. As expected, the pressure oscillations increase as the spatial resolution increases, and this phenomenon also affects the scheme with the acoustic damper term because of its reduced magnitude as h decreases (see Eq. (9)). Notwithstanding this, at each resolution, the scheme

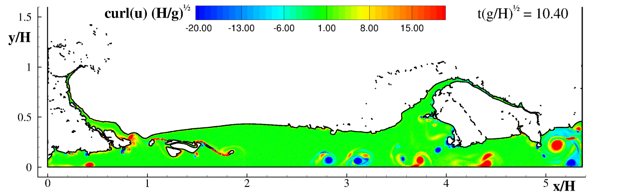

Fig. 11. Dam-break flow of a water column. $H/\Delta r = 400$, $\alpha = 0.005$, $\alpha_2 = 1.0$. Vorticity field during the splash-up stages at $t\sqrt{g/H} = 10.4$.

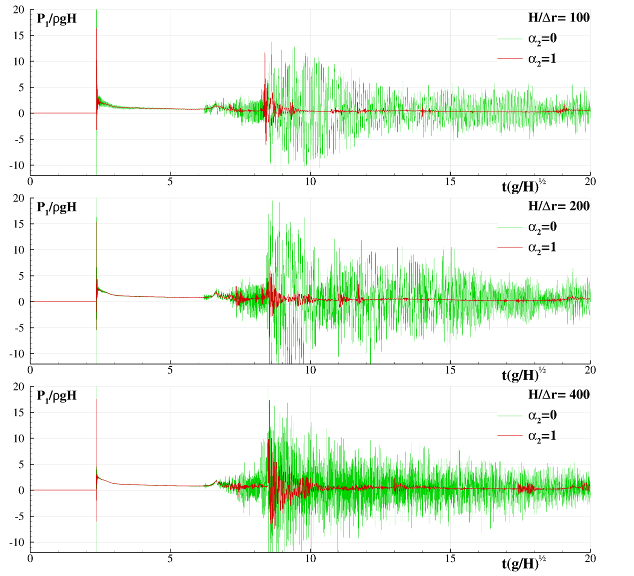

Fig. 12. Dam-break flow of a water column. Time histories of the pressure recorded at probe P_1 for different spatial resolutions. Cases with $\alpha_2 = 0$ and $\alpha_2 = 1$ refer to simulations without and with acoustic damper term respectively.

with the acoustic damper term shows a drastic reduction of the pressure oscillations in comparison to the scheme without it. A further dampening of this noise is possible by increasing the value of α_2 at the price of a smaller time step (see Section §II-A). Regarding the energy balance of the scheme, it is useful to define the potential energy difference $\Delta\mathcal{E}$ as the difference between the initial condition, when the liquid is at rest on the left of the dam, and the asymptotic final configuration, when

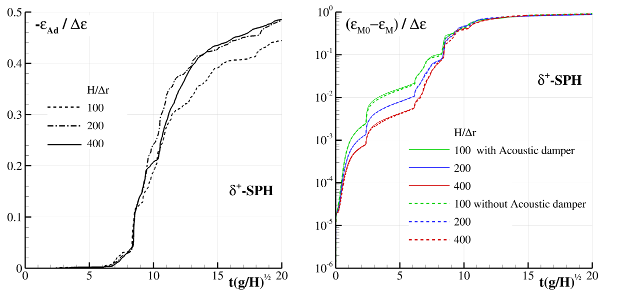

Fig. 13. Dam-break flow of a water column. Time histories of the energy dissipated by the acoustic damper term (left) and of the mechanical energy (right) for three different $H/\Delta r$ ratios.

the liquid is at rest in the whole tank:

$$\Delta\mathcal{E} := \mathcal{E}_{M0} - \mathcal{E}_{M\infty} = \rho\, g\, H^3 \left[1 - \frac{2H}{L}\right] \qquad (17)$$

The left panel of Figure 13 displays the behaviour of the energy dissipated by the acoustic damper term scaled by $\Delta\mathcal{E}$ for $H/\Delta r = 100, 200, 400$. Surprisingly, the amount of dissipated energy only shows minor changes. This is due to two opposite phenomena that partially compensate as the spatial resolution increases: i) the reduction of the magnitude of the acoustic damper term as h goes to zero, ii) the increase of the spurious acoustic noise. About the evolution of the global mechanical energy of the particle system, the right panel of Figure 13 shows that this is weakly influenced by the use of the acoustic damper term. This means that $\mathcal{E}_{diss}$ in Eq. (16) is approximately the same, implying that the energy dissipated by the acoustic damper, namely $\mathcal{E}_{ad}$, is replaced by the contributions $\mathcal{E}_V$ and $\mathcal{E}_N$ in the model without such a term. In any case, the action of the artificial viscosity and of the other numerical corrections is not enough to removed the acoustic waves generated during fluid-fluid and fluid-solid impacts. Before concluding, we would like to discuss a further aspect. Following the approach described in [15], it is possible to filter the pressure field of the δ^+-SPH during the post-processing stage and recover a numerical solution that is close to that obtained through the acoustic damper term. The proposed scheme, however, allows for a direct evaluation of a smooth pressure field and, therefore, is expected to be suitable for problems where the fluid is coupled with an elastic structure (see *e.g.* [36]–[38]). In particular, the action of the acoustic damper term helps to remove the spurious oscillations caused by the use of a numerical sound speed.

C. Water entry test

The last test is dedicated to the simulation of the vertical water entry of a wedge with a deadrise angle $\beta = 30°$. The parameters of this case are those of the case 4 in the experimental work of [39]. The wedge is freely dropped from a certain height and the touch down velocity is -2.5 m/s. The pressure on the wedge surface and its motions (penetration depth, velocity and acceleration) are measured. The δ-SPH is adopted for this test case with $c_0 = 25$ m/s. The coefficient of artificial viscosity is $\alpha = 0.01$ in all the simulations and the acoustic damper term is turned on or switched off by changing α_2 between 1 and 0. The minimum particle spacing close to the wedge is $L/\Delta x$=200 where L is the width of the wedge and the computational fluid domain is 2.0 m in width and 0.85 m in depth. Some snapshots of the pressure fields at different time instants are depicted in Fig. 14 from which one can clearly see that the pressure field obtained by using the acoustic damper term (left column) is always smoother in comparison with the scheme with α_2=0. As a quantitative validation, the time evolution of the pressure signal measured at the P4 probe, which is at 13 mm distance from the axis of symmetry of the wedge, is plotted on the left of Fig. 15. The average value of the pressure curve with and without acoustic damper are close to each other, but the one without acoustic damper shows more oscillations due to the acoustic waves, as observed in Figure 14. Both SPH simulations agree well with experimental data, which means that the acoustic waves only affect the local pressure signal but have negligible effect on the overall motion of the wedge.

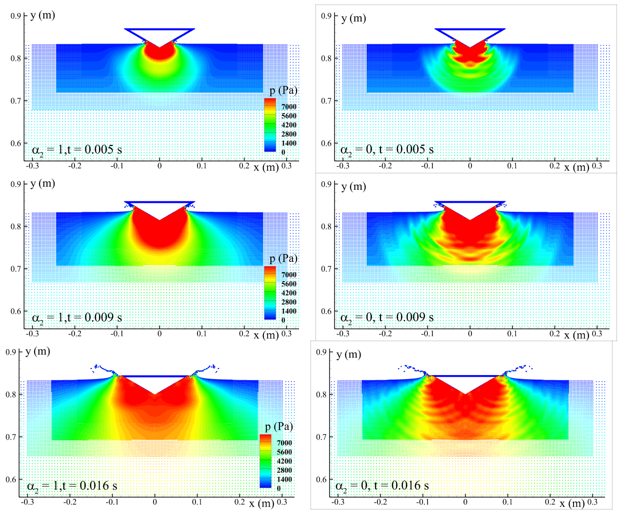

Fig. 14. Snapshots of the pressure field for the wedge water entry problem simulated by the δ-SPH model with $\alpha_2 = 1$ (left) and $\alpha_2 = 0$ (right).

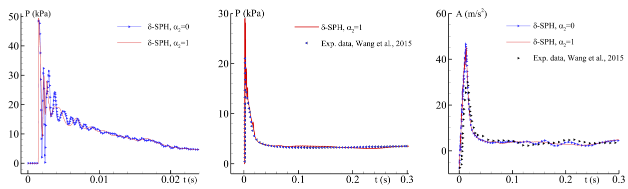

Fig. 15. Time evolution of the impact pressure simulated by δ-SPH with $\alpha_2 = 1$ and $\alpha_2 = 0$ (left); Comparison between the SPH solution and experimental data [39] for the impact pressure (middle); Time evolution of the acceleration predicted by δ-SPH with $\alpha_2 = 1$ and $\alpha_2 = 0$ and the comparison with experimental data [39] (right).

IV. Conclusions

An acoustic damper term is proposed to eliminate acoustic pressure waves in weakly-compressible SPH schemes. 2D numerical simulations carried out with the δ^+-SPH and δ-SPH models demonstrate that the proposed term is effective and provides a pressure field that is free from acoustic noise. This makes the numerical outputs similar to those obtained by using the incompressible variants of the SPH, retaining the advantages of the weakly-compressible models (i.e. avoiding the solution of a linear system associated with the Poisson equation for the pressure field). Convergence studies prove that, similar to other diffusive terms, the acoustic damper term converges to zero as the particle resolution increases, proving to be numerically consistent.

Acknowledgment

The work was partially supported by the SLOWD project which received funding from the European Union's Horizon

2020 research and innovation program under Grant No. 815044 and partially by the FUNBREAK-PRIN2017 project funded by the Italian Ministry MIUR under Grant Agreement No. 20172B7MY9 003. Dr. Peng-Nan Sun is funded by National Natural Science Foundation of China (Grant Nos. 12002404 & 51679053).

References

[1] J. Bonet Avalos, M. Antuono, A. Colagrossi, and A. Souto-Iglesias, "Shear-viscosity-independent bulk-viscosity term in smoothed particle hydrodynamics," *Phys. Rev. E*, vol. 101, p. 013302, Jan 2020. [Online]. Available: https://link.aps.org/doi/10.1103/PhysRevE.101.013302

[2] X. Cao, F. Ming, and A. Zhang, "Sloshing in a rectangular tank based on SPH simulation," *Applied Ocean Research*, vol. 47, pp. 241–254, 2014.

[3] M. S. Shadloo, G. Oger, and D. Le Touzé, "Smoothed particle hydrodynamics method for fluid flows, towards industrial applications: Motivations, current state, and challenges," *Computers & Fluids*, vol. 136, pp. 11–34, 2016.

[4] M. Green and J. Peiró, "Long duration SPH simulations of sloshing in tanks with a low fill ratio and high stretching," *Computers & Fluids*, vol. 174, pp. 179–199, 2018.

[5] C. Hermange, G. Oger, Y. Le Chenadec, and D. Le Touzé, "A 3d sph–fe coupling for fsi problems and its application to tire hydroplaning simulations on rough ground," *Computer Methods in Applied Mechanics and Engineering*, vol. 355, pp. 558–590, 2019.

[6] T. Ye, D. Pan, C. Huang, and M. Liu, "Smoothed particle hydrodynamics (SPH) for complex fluid flows: Recent developments in methodology and applications," *Physics of Fluids*, vol. 31, no. 1, p. 011301, 2019.

[7] J. Domínguez, G. Fourtakas, C. Altomare, R. Canelas, A. Tafuni, O. García-Feal, I. Martínez-Estévez, A. Mokos, R. Vacondio, A. J. Crespo *et al.*, "Dualsphysics: from fluid dynamics to multiphysics problems," *Computational Particle Mechanics*, pp. 1–29, 2021.

[8] M. Luo, A. Khayyer, and P. Lin, "Particle methods in ocean and coastal engineering," *Applied Ocean Research*, vol. 114, p. 102734, 2021.

[9] A. Colagrossi and M. Landrini, "Numerical simulation of interfacial flows by smoothed particle hydrodynamics," *J. Comp. Phys.*, vol. 191, pp. 448–475, 2003.

[10] M. Antuono, A. Colagrossi, S. Marrone, and D. Molteni, "Free-surface flows solved by means of SPH schemes with numerical diffusive terms," *Computer Physics Communications*, vol. 181, no. 3, pp. 532–549, 2010.

[11] J. Vila, "On particle weighted methods and smooth particle hydrodynamics," *Mathematical models and methods in applied sciences*, vol. 9, no. 02, pp. 161–209, 1999.

[12] K. Gong, H. Liu, and B. Wang, "Water entry of a wedge based on SPH model with an improved boundary treatment," *Journal of Hydrodynamics*, vol. 21, no. 6, pp. 750–757, 2009.

[13] P. Sun, F. Ming, and A. Zhang, "Numerical simulation of interactions between free surface and rigid body using a robust SPH method," *Ocean Engineering*, vol. 98, pp. 32–49, 2015.

[14] P. Sun, A. Zhang, S. Marrone, and F. Ming, "An accurate and efficient SPH modeling of the water entry of circular cylinders," *Applied Ocean Research*, vol. 72, pp. 60–75, 2018.

[15] D. Meringolo, A. Colagrossi, S. Marrone, and F. Aristodemo, "On the filtering of acoustic components in weakly-compressible SPH simulations," *Journal of Fluids and Structures*, vol. 70, pp. 1–23, 2017.

[16] P. Sun, A. Colagrossi, S. Marrone, M. Antuono, and A. Zhang, "A consistent approach to particle shifting in the δ-plus-sph model," *Computer Methods in Applied Mechanics and Engineering*, vol. 348, pp. 912–934, 2019.

[17] M. Antuono, P. Sun, S. Marrone, and A. Colagrossi, "The δ-ALE-SPH model: An arbitrary Lagrangian-Eulerian framework for the δ-SPH model with particle shifting technique," *Computers & Fluids*, vol. 216, p. 104806, 2021.

[18] S. Marrone, A. Colagrossi, A. Di Mascio, and D. Le Touzé, "Analysis of free-surface flows through energy considerations: Single-phase versus two-phase modeling," *Phys. Rev. E*, vol. 93, p. 053113, May 2016. [Online]. Available: http://link.aps.org/doi/10.1103/PhysRevE.93.053113

[19] M. Antuono, S. Marrone, A. Di Mascio, and A. Colagrossi, "Smoothed particle hydrodynamics method from a large eddy simulation perspective. Generalization to a quasi-Lagrangian model," *Physics of Fluids*, vol. 33, no. 1, p. 015102, 2021.

[20] H. Wendland, "Piecewise polynomial, positive definite and compactly supported radial functions of minimal degree," *Adv. Comput. Math.*, vol. 4, no. 4, pp. 389–396, 1995. [Online]. Available: http://dx.doi.org/10.1007/BF02123482

[21] A. Colagrossi, D. Durante, J. Bonet Avalos, and A. Souto-Iglesias, "Discussion of Stokes' hypothesis through the smoothed particle hydrodynamics model," *Phys. Rev. E*, vol. 96, p. 023101, Aug. 2017.

[22] M. Antuono, A. Colagrossi, and S. Marrone, "Numerical diffusive terms in weakly-compressible SPH schemes," *Computer Physics Communications*, vol. 183, no. 12, pp. 2570–2580, 2012.

[23] P. Sun, A. Colagrossi, S. Marrone, M. Antuono, and A. Zhang, "Multi-resolution Delta-plus-SPH with tensile instability control: Towards high reynolds number flows," *Computer Physics Communications*, vol. 224, pp. 63–80, 2018.

[24] S. Marrone, A. Colagrossi, D. L. Touzé, and G. Graziani, "Fast free-surface detection and level-set function definition in SPH solvers," *Journal of Computational Physics*, vol. 229, no. 10, pp. 3652–3663, 2010.

[25] J. Swegle, D. Hicks, and S. Attaway, "Smoothed particle hydrodynamics stability analysis," *Journal of Computational Physics*, vol. 116, pp. 123–134, 1995.

[26] W. Dehnen and H. Aly, "Improving convergence in smoothed particle hydrodynamics simulations without pairing instability," *Monthly Notices of the Royal Astronomical Society*, vol. 425, no. 2, pp. 1068–1082, 2012. [Online]. Available: http://dx.doi.org/10.1111/j.1365-2966.2012.21439.x

[27] J. Monaghan, "Smoothed Particle Hydrodynamics," *Reports on progress in physics*, vol. 68, no. 8, p. 1703, 2005.

[28] ——, "SPH without a tensile instability," *J. Comp. Phys.*, vol. 159, no. 2, pp. 290–311, 2000.

[29] A. Khayyer, H. Gotoh, and Y. Shimizu, "Comparative study on accuracy and conservation properties of two particle regularization schemes and proposal of an optimized particle shifting scheme in isph context," *Journal of Computational Physics*, vol. 332, pp. 236–256, 2017.

[30] M. Antuono, S. Marrone, A. Colagrossi, and B. Bouscasse, "Energy balance in the δ-SPH scheme," *Computer Methods in Applied Mechanics and Engineering*, vol. 289, pp. 209–226, 2015.

[31] D. Meringolo, S. Marrone, A. Colagrossi, and Y. Liu, "A dynamic δ-SPH model: How to get rid of diffusive parameter tuning," *Computers & Fluids*, vol. 179, pp. 334–355, 2019.

[32] J. Cercos-Pita, M. Antuono, A. Colagrossi, and A. Souto-Iglesias, "SPH energy conservation for fluid–solid interactions," *Computer Methods in Applied Mechanics and Engineering*, vol. 317, pp. 771–791, 2017.

[33] S. Marrone, A. Colagrossi, A. Di Mascio, and D. Le Touzé, "Prediction of energy losses in water impacts using incompressible and weakly compressible models," *Journal of Fluids and Structures*, vol. 54, pp. 802–822, 2015.

[34] S. Marrone, M. Antuono, A. Colagrossi, G. Colicchio, D. Le Touzé, and G. Graziani, "δ-SPH model for simulating violent impact flows," *Computer Methods in Applied Mechanics and Engineering*, vol. 200, no. 13-16, pp. 1526–1542, 2011.

[35] L. Lobovský, E. Botia-Vera, F. Castellana, J. Mas-Soler, and A. Souto-Iglesias, "Experimental investigation of dynamic pressure loads during dam break," *Journal of Fluids and Structures*, vol. 48, pp. 407–434, 2014.

[36] P. Sun, D. Le Touzé, and A. Zhang, "Study of a complex fluid-structure dam-breaking benchmark problem using a multi-phase SPH method with APR," *Engineering Analysis with Boundary Elements*, vol. 104, pp. 240–258, 2019.

[37] P. Sun, D. Le Touzé, and A. Oger, G.and Zhang, "An accurate FSI-SPH modeling of challenging fluid-structure interaction problems in two and three dimensions," *Ocean Engineering*, vol. 221, p. 108552, 2021.

[38] Z.-F. Meng, A.-M. Zhang, J.-L. Yan, P.-P. Wang, and A. Khayyer, "A hydroelastic fluid–structure interaction solver based on the riemann-sph method," *Computer Methods in Applied Mechanics and Engineering*, vol. 390, p. 114522, 2022.

[39] J. Wang, C. Lugni, and O. M. Faltinsen, "Experimental and numerical investigation of a freefall wedge vertically entering the water surface," *Applied Ocean Research*, vol. 51, pp. 181–203, 2015.